CHAPTER 4

Three-dimensional radiative transfer simulations

Several approaches have been invented to solve the RT equation. The solution methods may be divided into two groups. The first group is based on an analytical transformation of the RT equation into a form which allows the solutions of the transformed equation. Among those methods are: 1) the matrix operator method (*Plass et al.*, 1973; *Fell and Fischer*, 2001; *Schröder et al.*, 2003), 2) discrete ordinates (*Stamnes et al.*, 1988), and 3) invariant embedding (*Mobley*, 1994). In all cases, the vertical variability of atmospheric parameters relevant for RT need to be approximated by a certain amount of layers. The layers are assumed to be homogeneous in horizontal directions. Probably the only exception is an extended discrete ordinate method from *Evans* (1998) (SHDOM), which is applicable two 3d input fields and numerically effective. The second group is called Monte Carlo methods. Monte Carlo methods are the most general technique for a numerical solution of the radiative transfer equation. Especially, they are applicable to 3d RT problems with arbitrary optical properties and without any assumptions or simplifications. Even though the Monte Carlo method is time consuming for optical thick and spatially large fields, the 3d RT simulations in this work are conducted by this method.

The Monte Carlo model used in this work is based on a model described by *Petty* (1994). It relies on classical Monte Carlo methods and was extended by the author to account for local estimates. The next section introduces these two Monte Carlo methods. Afterwards statistical aspects of the random nature of Monte Carlo methods and their impact on the accuracy of nadir reflectances is evaluated. Finally, the last part gives the validation of the model.

4.1. Classical Monte Carlo methods and local estimates

The Monte Carlo method used for this study is a forward tracing model. In such a model the photons are inserted at the top of the atmosphere and traced until they are absorbed or hit a boundary without being reflected. The propagation of each photon is governed by a set of probability functions. These functions depend upon the physical processes and the type of particle which causes the process. They control the distance each photons travels to the next interaction, the outcome of the interaction (either scattering or absorption) and the new direction of propagation. According to the scientific demands and the required accuracies the model domain is divided into grid boxes, each characterised by specific probability functions and optical parameters. The first half of this section concentrates on the explanation of the Monte Carlo method and the derivation of the probability functions and optical parameters required to run such a model. The outline is oriented at *Mobley* (1994). The second half introduces a variance reduction techniques, the so called local estimates.

After the photon was inserted into the model domain and after each scattering event, it is assigned an optical path length τ which describes the optical length it travels before the next scattering event occurs and a new τ is assigned. The probability p of the photon being absorbed or scattered between τ and $\tau+\mathrm{d}\tau$ is given by Lambeer's Law, $p\mathrm{d}\tau = \exp(-\tau)\mathrm{d}\tau$. Integrating this from zero to infinity equals one and therefore confirms the requirements for a probability density function. The probability P that the photon is absorbed or scattered between $\tau = 0$ and τ is determined by the cumulative distribution function, $P = 1 - \exp(-\tau)$. The aim is to use a randomly drawn R_τ to calculate a value for τ. R_τ is a random

number equally distributed between zero and one. Its probability density function is one for values within the interval [0,1] and zero elsewhere. In order to apply such an approach the probability that R_τ lies in the interval $R_\tau + \mathrm{d}R_\tau$ need to be identical to the probability that τ is within $\tau + \mathrm{d}\tau$. In consequence, both cumulative frequency distributions are identical and one gets: $R_\tau = 1 - \exp(-\tau)$. It follows with $1 - R_\tau$ being equally distributed between zero and one:

$$\tau = -\ln R_\tau. \tag{4.1}$$

If the random number R_τ is given, the optical path length of the photon between two interactions, either absorption or scattering, can be determined. By the subdivision of the model domain in grid boxes each box has to be assigned the volume extinction coefficient. The optical path of the photon is then accumulated during its propagation through the model domain until its optical path becomes larger than τ. If the accumulated path is larger than τ and if the photon has not reached the upper or lower boundary, a scattering or an absorption event occurs. Then, a new τ is calculated using Eq. 4.1. In this model periodic boundary layers are applied.

In case of a scattering event the new propagation direction needs to be determined. Each photon is characterised by its location and flight direction. The probability of the photon being scattered in a new direction is given by the product of the phase function $\tilde{\beta}$ and the solid angle centred around the new direction. $\tilde{\beta}$ generally depends on the zenith and azimuth angle (θ and ϕ, respectively), both defining the new direction of the photon in a coordinate system centred on the direction of the incident photon. It can be assumed that θ and ϕ are independent variables, since in the atmosphere the phase function typically depends on θ only. Therefore, θ is interpreted as the scattering angle ψ, and the probability of the photon being scattered in the new direction can be interpreted as a product of the probability density functions for the scattering and azimuth angle, p_ψ and p_ϕ, respectively:

$$\tilde{\beta}(\psi;\phi)\sin\psi \mathrm{d}\psi \mathrm{d}\phi = p_\psi \mathrm{d}\psi p_\phi \mathrm{d}\phi. \tag{4.2}$$

Since the azimuth angle is uniformly distributed in the interval [0, 2π], one gets that p_ψ is equal to $2\pi\tilde{\beta}\sin\psi$. Similar to the previous procedure, the cumulative distribution function is determined and can be related to a new random number R_ψ being equally distributed between 0 and 1 (recall the normalisation of the phase function in equation 1.3):

$$R_\psi = 2\pi \int_0^\psi \tilde{\beta}(\psi)\sin\psi \mathrm{d}\psi. \tag{4.3}$$

The inverse cumulative distribution function needs to be provided at each grid box. This function directly relates the random number R_ψ to the scattering angle ψ. An exemplary phase function and its inverse cumulative phase function is shown in Figure 4.1. Note, how the strongly peaked forward scattering part of the phase function is transformed into a very slow increase of the inverse cumulative phase function. The consequence is that for a large amount of different R_ψ the related scattering angle is almost constant and in forward direction. The phase function and its inverse cumulative are calculated for 100,000 discrete, equidistant values of ψ.

If a similar approach is applied to the azimuth angle ϕ it yields:

$$\phi = 2\pi R_\phi \tag{4.4}$$

with R_ϕ being a third random number equally distributed between 0 and 1. If both angles are known the new flight direction of the photon can be calculated.

The knowledge of the path of all photons through the medium opens a direct way to calculate photon path length statistics: The determination of the geometrical path l between two scattering events, τ/σ_{ext}, and a successive summation of these paths for each photon provide the probability density function of the photon path lengths, $P(l)$. $P(l)\mathrm{d}l$ gives the probability that the photon has travelled a geometrical path between $l + \mathrm{d}l$. The integral over $P(l)\mathrm{d}l$ must equal unity. Due to numerical constrains the geometrical path is divided

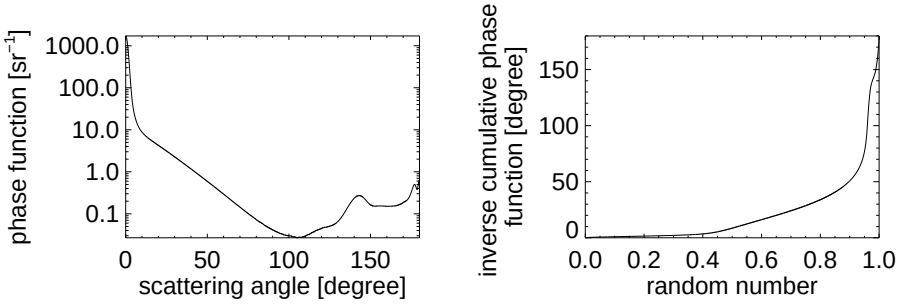

FIGURE 4.1. Phase function versus scattering angle (left panel) and the corresponding inverse cumulative phase function as a function of random number (right panel). This example is based on drop size distributions given by *Deirmandjian* (1969) and Mie calculations.

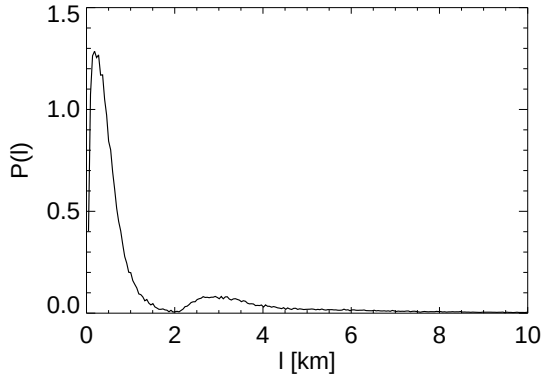

FIGURE 4.2. Probability density function of photon path length versus geometrical path. $P(l)$ is determined at an exemplary grid box of the computations presented in section 5.3.

in 1000 bins with increments depending on the sun zenith angle θ_0, e.g. 0.04 km for θ_0=0°. An exemplary $P(l)$ is presented in Figure 4.2. The artificial cloud, which forms the basis for the determination of the given result, is described in section 5.3. The cloud top is at 1 km and the surface albedo is set to 0.4. Most of the photons are scattered at the top of the cloud which explains the peak of $P(l)$ at small photon paths. The location of the maximum is slightly larger than the mean free photon path, $1/\tau$=0.1 km. The second maximum is due to reflection of photons at the surface. Its theoretical position can be determined by $(1 + 1/\cos(\theta_0))$ * cloud top height = 2.3 km ($\theta_0 = 38.6°$ is the sun zenith angle).

Each time the photon encounters a scattering or an absorption event, it has to be decided which of both events actually occurs. In case of absorption, the photon will never reach the detector. This is computationally inefficient and can be avoided by a new interpretation of the inserted photons: Each photon is not considered as a single photon but as a packet of photons which is assigned to a weight $w = 1$ before it is inserted. Every time a scattering event occurs, the weight of the photon is multiplied with the single scattering albedo ω_0. The multiplication can be interpreted as follows: The fraction $1 - \omega_0$ of the photon packet is absorbed and ω_0 will be scattered in a new direction. A photon packet is traced until its weight drops below 10^{-7}.

Despite the above mentioned effort the majority of photons are still ineffective because they don not intercept with a detector of specific field of view. The photons are detected

dependent on their flight direction given by the zenith and the azimuth angle (θ and ϕ, respectively). In all subsequent computations, these two angles are binned in boxes of 2°x6°, the former corresponding to the zenith and the latter to the azimuth angle. All photons not leaving the upper boundary within the field of view of the detector don not contribute to the signal. Having in mind the random nature of the Monte Carlo method, it follows, that a very large amount of photons is required to reduce the noise level significantly. The original version of the model utilised in this work was a backward tracing model developed by *Petty* (1994). It was converted to a forward tracing model and adapted to solar radiative transfer by Ralf Bennartz. Henceforth, the model is named *classical Monte Carlo model*.

To reduce the noise level variance reduction techniques can be applied. Among them is the so called local estimate method (*Marchuk et al.*, 1980). The underlying idea of the local estimate method is that every scattering contributes to the signal measured at a specific detector position. If the scattering angle ψ is defined as the angle between incident direction and the direction to the detector, the probability of the photon being scattered in the direction of the detector can be calculated by simply multiplying the photon weight and the phase function value at ψ. In this case, the product need to be transmitted from the scattering event to the detector which can be done by an exponential decay given the direct path and the volume extinction of each box along the path. In this way, the contribution of every scattering event into the detector is accumulated. The last step is the normalisation of the signal on the amount of inserted photons. Thus, the radiance L at a specific location $(x; y)$ at the top of the atmosphere can be determined as follows:

$$L(x;y) = 1/N_{ph} \sum_j \left(\tilde{\beta}(\psi)_j w_j \left(\prod_i \exp\left(-\tau_i\left(j\right)\right)\right)\right) \tag{4.5}$$

with i being an index of the traversed boxes, τ_i the corresponding optical path length, j an index of the scattering events and N_{ph} the amount of photons inserted in $(x; y)$. In particular, reflection at the surface is considered as a scattering event with a scattering probability of $\cos\theta_z/\pi$ (θ_z: angle between direction of propagation and z-axis). This approach to calculate RT is named *local estimate model* in the following and was implemented by the author.

The Monte Carlo simulations yield the reflectance, defined as follows:

$$R(x;y;\theta;\phi) = \frac{\pi L(x;y;\theta;\phi)}{F_0 \mu_0} \tag{4.6}$$

with F_0 being the incident solar irradiance and μ_0 the cosine of the sun zenith angle.

An advantage of the *local estimate model* is that it offers a simple approach to derive a (multiple-scattering) weighting function. The weighting function provides the user with information of the origin of the radiation, e.g. most of the signal comes from layers close to cloud top while lower layers contribute less. Each layer can be assigned a weight which gives the relative contribution of this layer to the integrated radiation, $R = \sum \mathrm{weight\,(z)}$. In order to determine the weighting function, $L(x; y)$ is summed for each scattering event in every grid box. In other words: Eq. 4.5 is considered to be height dependent. The current version of the *local estimate model* allows the determination of the weighting function for nadir viewing and single columns only. An example is given in Figure 6.4b. Other approaches to retrieve the weighting function were introduced by *Platnick* (2000).

In summary, the inverse cumulative phase function, the volume extinction coefficient, and the single scattering albedo need to be provided at every grid box of the model domain as input for the *classical Monte Carlo model*. In addition, the *local estimate model* requires the normalised phase function (equation 1.3) and RT calculations in double precision (see section 4.5).

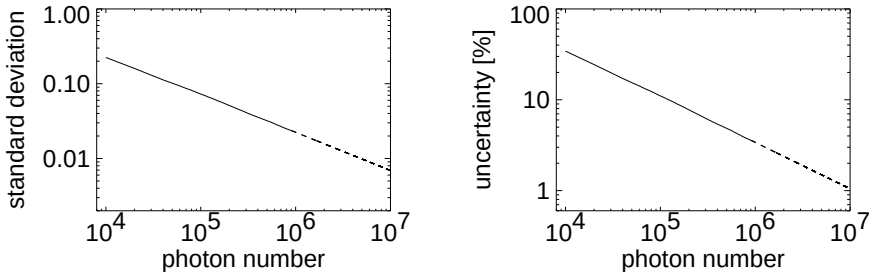

FIGURE 4.3. Standard deviation (left panel) and uncertainty (right panel) versus photon number. The results are extrapolated to a photon number of 10^7 (dashed lines).

4.2. The equivalence theorem

The equivalence theorem provides a powerful and widely applicable approach to calculate spectral high-resolution reflectances and was introduced by *Irvine* (1964). It directly relates the reflectances simulated in non-absorbing spectral ranges to reflectances within absorption lines.

The equivalence theorem can be written as follows:

$$R(\omega_0 \neq 1; \lambda) = R(\omega_0 = 1) \int_0^\infty P(l) \exp\left(-\sigma_a\left(\lambda\right) l\right) \mathrm{d}l, \tag{4.7}$$

if the geometry and the scattering properties of the medium as well as detector position and illumination do not change. From the *classical Monte Carlo model* one gets the photon statistics and the nadir reflectance in a window channel, $P(l)$ and $R(\omega_0 = 1)$, respectively. The spectral high-resolution volume extinction coefficient of gas absorption, $\sigma_a\left(\lambda\right)$, can be calculated with the modified k-distribution presented by *Bennartz and Fischer* (1999). The spectral resolution should be high enough to allow monochromatic calculations.

The equivalence theorem is independent of any assumptions and can deal with media of arbitrary geometry. One single RT calculation is required to derive the photon statistics and reflectance, and the entire, highly resolved reflection spectrum is received from this single simulation. The utility and a verification of the equivalence theorem is given in *Stephens and Heidinger* (2000).

4.3. Uncertainty estimation of the *classical Monte Carlo model*

The photon trajectory through the model domain is determined with the help of three independent, randomly chosen parameters. The random nature of the *classical Monte Carlo model* and the loss of the majority of photons which don not reach the detector, introduce noise to the simulated reflectance. In the literature a wide range of photon numbers (from 10^6 to $8\mathrm{x}10^8$) are used to calculate the reflectance with Monte Carlo methods. Here, the statistical significance of the reflectance simulated with the *classical Monte Carlo model* and an appropriate photon number for these simulations will be discussed.

To test the statistical significance Monte Carlo simulations were conducted using highly inhomogeneous cloud fields, as they were discussed in sections 3.1 and 3.4. The parameters discussed in section 5.1 were chosen but for a reduced model domain size of 32x32 pixels and for a sun at zenith. Ten simulations were performed with 10^6 photons, and interim results are saved every 10,000 photons. For each interim result the standard deviation σ and the mean $\langle R \rangle$ are determined. The uncertainty of the *classical Monte Carlo model* is deduced by the ratio of these two values: $\sigma / \langle R \rangle$.

Figure 4.3 shows the results of the analysis: standard deviation and uncertainty versus number of photons. The dashed line gives the extrapolation to 10^7 photons. The slope of

the standard deviation is proportional to $N_{ph}^{-1/2}$ which exactly meets theoretical expectations: Assuming that the photon path can be considered as a Bernoulli trial, the standard deviation of the reflectance is expected to be proportional to $N_{ph}^{-1/2}$ (*Spanier and Gelbard*, 1969). This plus the smooth appearance of the slope makes the interpolation to 10^7 photons reliable. At 10^7 photons the uncertainty of the *classical Monte Carlo model* reaches 1%. If not averages but local values are considered, the uncertainty of the reflectance varies between 0.4% and 2%. Furthermore, the uncertainty depends on the viewing geometry, i.e. the zenith angle of the sun and of the observer. The uncertainty related to viewing direction reaches maximum 1%, if the signals are azimuthally averaged, and 13%, if averaging is not carried out. Over large ranges of viewing direction the uncertainty is almost constant and significantly smaller. The dependence on sun zenith angle is discussed in detail in *Barker and Davies* (1992) and found to be significant.

The presented uncertainty analysis is not of general validity. In addition to a dependence on sun zenith angle, the uncertainty will depend on the considered (broken) cloud field and especially on the mean optical thickness and surface albedo. E.g., if it can be assumed that these parameters do not effect the standard deviation, the increase in mean reflectance for increasing optical thickness or surface albedo will decrease the uncertainty. However, this discussion sensitises the question for an appropriate amount of photon numbers. If simulations are performed conducting the *classical Monte Carlo model*, 10^7 photons are used.

The *local estimate model* is not subjected to such uncertainty estimations although it has a random nature. In general, it is far more effective than the *classical Monte Carlo model*: It has predefined detector fields so that every scattering event contributes to the reflectance, so no photon is lost. The efficiency decreases, if the mean optical thickness increases because the contributions of the scattering events are more subsided, see Eq. 4.5. Another aspect affecting the accuracy of the *local estimate model* is the strength of the forward peak of the phase function. If the randomly defined scattering angle happens to be in the forward direction, one large single contribution is added to the interim result of the reflectance. Since this event is rare and all other contributions are significantly smaller, a large amount of scattering events is needed to reduce the uncertainty. The *local estimate model* will be validated in section 4.5. Every time the *local estimate model* is used, an uncertainty discussion is given.

4.4. Representativity of a single cloud realisation

Not only the Monte Carlo methods are based on stochastic processes but also the cloud generators discussed in the previous sections. The question arises, if different cloud realisations yield statistically identical reflectance fields. The following investigations are conducted with the *classical Monte Carlo model* and based on clouds described in section 4.3.

Ten cloud fields are generated, and each of the fields is based on a different set of random variables. The resulting fields are characterised by identical average optical thicknesses and corresponding standard deviations but by different configurations. The number of photons per horizontal box is 10^7, to achieve an accuracy of approximately 1%. Utilising all ten simulations the difference among each other is calculated by the ratio of the standard deviation and the average reflectance. The result reveals a difference of 0.5%. Therefore, a single cloud realisation can be considered as statistical significant as it is significantly smaller than the uncertainty of the model.

4.5. Validation of the *local estimate model*

To investigate the accuracy and applicability of the *local estimate model*, the Intercomparsion of 3d Radiation Codes (I3RC) is consulted. A wide variety of RT codes is applied to a well defined set of input fields, which present the earth-atmosphere system by various degrees of complexity. A few radiometric parameters and their statistical characteristics

TABLE 4.1. Overview of experiments used for the validation of the *local estimate model.*

Phase	Case	Experiments	Abbreviations
1	1d	1-4	p1c1_e1-4
1	2d	3, 6-8	p1c2_e3,6-8
2	cumulus (Cu), 3d	1-2, 6-7	p2cu_e1-2,6-7
2	stratocumulus (Sc), 3d	7	p2sc_e7

form the basis of the intercomparison. The main aim is to achieve an improvement of climate models and remote sensing. The I3RC provides an excellent opportunity to identify errors and limits and therefore helps to debug the model. More details on I3RC can be found on the following web-page: http://i3rc.gsfc.nasa.gov.

The intercomparison is structured in three phases. Phase 1 aims at the identification of errors and limits as well as debugging. Phase 2 focuses on timing comparisons. Phase 3 extends the computations, guides improvements and shares the state-of-the art RT code with public users.

Here, the I3RC is used to validate and debug the *local estimate model*. The large amount of available validation experiments is reduced to focus on output values relevant for the studies presented in this work. The remaining experiments cover all relevant situations to allow a successful validation. An overview of the considered experiments is given in Table 4.1.

In total 13 validation experiments are carried out. Each of it considers periodic boundary conditions, monochromatic computations, and neglects emission. The phase1 case1 experiments utilise a 1d, academical step function: 16 pixels with an optical thickness of 2 are adjacent to 16 pixels of an optical thickness of 18. The size of each pixel is 0.5/32 km times 0.25 km. The experiments are set up by a variation of θ_0 and ω_0:

1) θ_0=0°, ω_0=1
2) θ_0=60°, ω_0=1
3) θ_0=0°, ω_0=0.99
4) θ_0=60°, ω_0=0.99

During phase1 case 2, a 2d cloud field derived from cloud radar and microwave radiometer stationed at the ARM CART site are supplied. The cloud field comprises of 640 pixels along the x-axis and 54 pixels in the vertical with resolutions of 0.05 and 0.045 km, respectively. Two different phase functions are considered: the Henyey-Greenstein function $\tilde{\beta}_{HG}$ with g=0.85 and the phase function after *Deirmandjian* (1969), $\tilde{\beta}_{C1}$. The conducted experiments are (A: surface albedo):

3) θ_0=0°, ω_0=0.99, A=0, $\tilde{\beta} = \tilde{\beta}_{HG}$
6) θ_0=0°, ω_0=1, A=0, $\tilde{\beta} = \tilde{\beta}_{C1}$
7) θ_0=60°, ω_0=1, A=0, $\tilde{\beta} = \tilde{\beta}_{C1}$
8) θ_0=60°, ω_0=1, A=0.4, $\tilde{\beta} = \tilde{\beta}_{C1}$

Phase2 of the validation process considers 3d cloud fields and partly molecule and aerosol extinction. It is separated into computations on the basis of a 3d stratocumulus (Sc) and cumulus (Cu) cloud field, both simulated with an LES model. The domain of Sc consists of 64x64x34 pixels with a horizontal and vertical resolution of 0.055 and 0.025 km, respectively. The Cu extends over 100x100x62 pixels with respective resolutions of 0.0667 and 0.04 km. The input fields of σ_{ext} and ω_0 are provided on the web-page while the provided phase functions are related to a specific radius. The provided data sets cover a maximum height of 30 km which needs to be resolved by equidistant box sizes of thickness 0.025 or 0.04 km. In order to reduce computational efforts, the maximum domain height

TABLE 4.2. Summary of the outcome of the validation experiments. The mean $\langle R \rangle$, the standard deviation σ_R, and the skewness γ_R of reflectance R as computed by the *local estimate model* and MYSTIC are confronted with each other.

Experiment	$\langle R \rangle$	$\langle R \rangle$ MYSTIC	σ_R	σ_R MYSTIC	γ_R	γ_R MYSTIC
p1c1_e1	0.2555	0.2568	0.1698	0.1690	0.0963	0.0922
p1c1_e2	0.4050	0.4069	0.2987	0.2972	0.1396	0.1355
p1c1_e3	0.2003	0.2015	0.1296	0.1292	0.0911	0.0879
p1c1_e4	0.3216	0.3230	0.2369	0.2355	0.1551	0.1526
p1c2_e3	0.3916	0.3923	0.0727	0.0740	-0.3574	-0.3124
p1c2_e6	0.6974	0.6645	0.1685	0.1699	0.1579	0.1656
p1c2_e7	0.5259	0.5271	0.1367	0.1378	0.3971	0.4499
p1c2_e8	0.6004	0.6019	0.1079	0.1073	0.5318	0.5597
p2cu_e1	0.2979	0.2959	0.1541	0.1511	2.0311	2.0641
p2cu_e2	0.2373	0.2374	0.1964	0.1971	2.3966	2.4049
p2cu_e6	0.2899	0.2860	0.1450	0.1365	2.0205	2.1187
p2cu_e7	0.2419	0.2448	0.1699	0.1662	2.8073	2.7798
p2sc_e7	0.3578	0.3598	0.1355	0.1240	0.1511	0.1695

is made smaller: σ_{ext} and σ_b above 1.815 km (Sc) and 2.4 km (Cu), the level of maximum cloud top, were scaled to a single layer of 0.025 km (Sc) and 0.04 km (Cu) thickness by dividing the integral over height by the single layer thickness. ω_0 is calculated by their ratio. It is left to the user to calculate appropriate phase functions at every grid box. To avoid a maximum total amount of 6.2x10^5 phase functions, the domain was divided into four major regions: 1) boxes below cloud base, 2) cloudy boxes, 3) cloud free boxes (above cloud base and cloud free columns) and 4) boxes above maximum cloud top. $\tilde{\beta}$ is calculated according to:

$$\tilde{\beta} = \sum_i \frac{\sigma_b^i \tilde{\beta}^i}{\sigma_b}. \tag{4.8}$$

First, the local phase function is determined using Eq. 4.8 with i being an index referring to the scattering types (molecules, aerosols, or cloud droplets) and σ_b being the corresponding total volume scattering coefficient. Then, spatial averaging is carried out using the same equation but with i being an index of the boxes belonging to the four categories defined above. Four experiments of phase2 were utilised: experiments 1 and 2, each without atmosphere, and experiments 6 and 7, each including atmosphere, and experiments 1 and 6 as well as 2 and 7 with θ_0=0° and 60°, respectively. A=0.2 in all experiments.

In all cases the validated parameter is the nadir reflectance. The validation is carried out in terms of the first three moments of R: mean $\langle R \rangle$, standard deviation σ_R, and skewness γ_R. Table 4.2 summarises the outcome of the validation experiments. The first column specifies the experiment, see Table 4.1 for an explanation of the abbreviations. The next six columns are divided in pairs, one pair for each moment: In each pair the first value corresponds to the *local estimate model* and the second to MYSTIC. MYSTIC is a Monte Carlo model and part of the model package libRadtran, available online at http://www.libradtran.org. The performance of MYSTIC within I3RC is documented in *Mayer* (1999), *Mayer* (2000) and on the I3RC homepage.

All moments are in excellent agreement with the results received by MYSTIC and are well within the range defined by all models which participated in I3RC. There are only two exceptions: $\langle R \rangle$ for p2cu_e7 and p2sc_e7. Here, the values of MYSTIC define the lower boundary of results presented on the I3RC homepage. However, the difference is only 1.2% and 0.6%, respectively. The simulated nadir reflectance fields corresponding to the

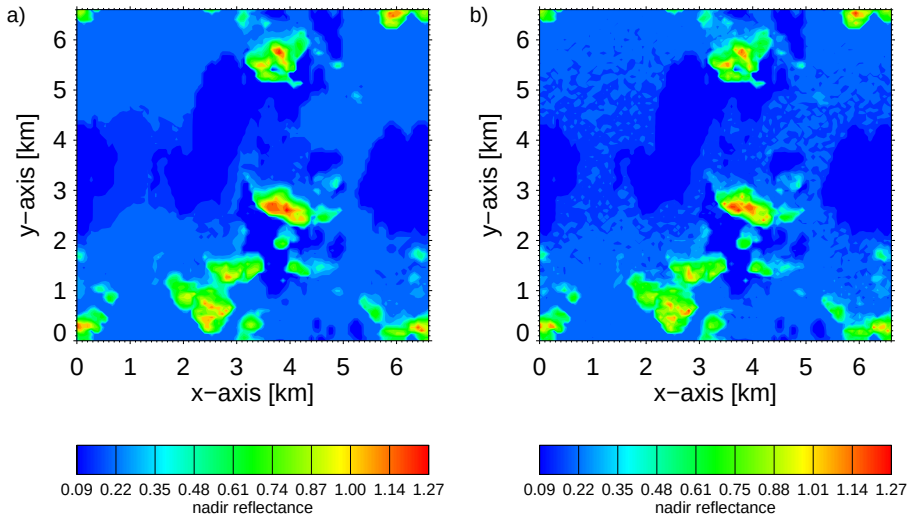

FIGURE 4.4. Nadir reflectance as computed by the *local estimate model* (Fig. a) and MYSTIC (Fig. b). The range of the colour bar is kept fixed in both figures. The simulation is based on experiment p2cu_e7.

experiment of largest relative discrepancy, p2cu_e7, are shown in Figure 4.4: Figure 4.4a for the *local estimate model* with $2.5\text{x}10^9$ photons) in total and Figure 4.4b for MYSTIC. The colour bar covers a constant range in both cases and is oriented at the reflectance range of the *local estimate model*. The minimum reflectances of both simulations agree very well but the maximum reflectance of MYSTIC is 1.23 and not 1.27.

Looking at R over surfaces the values of MYSTIC are characterised by a much stronger variability, almost patchy-like in appearance. The reason is a significantly higher noise level. If averages of R for values smaller than 0.25 are considered, a difference of a few percent is found and may give reason for the discrepancy.

During the validation experiment, bugs were removed and significant improvements were carried out: 1) The cumulative phase function needs to be provided in discrete steps. Having its strong maximum at back scatter directions in mind (see Figure 4.1b), the large amount of discrete bins, 10^5, becomes reasonable. 2) At each scattering event, the contribution to the local reflectance is calculated by an exponential decrease of the scattered light (see Eq. 4.5). This requires double precision to achieve a satisfactory accuracy. 3) The reflection at the surface must be considered as a scattering event with a scattering probability of $\cos\theta/\pi$ with θ being the angle of incidence.

To summarise, a successful validation was carried out. The I3RC has turned out to be an excellent platform to identify bugs and validate RT models.